

Dynamics of stars around spiral arms in an N-body/SPH simulated barred-spiral galaxy

Robert J.J. Grand ^{1*}, Daisuke Kawata ¹, Mark Cropper ¹

¹ *Mullard Space Science Laboratory, University College London, Holmbury St. Mary, Dorking, Surrey, RH5 6NT*

1 March 2012

ABSTRACT

We run N-body smoothed particle hydrodynamics (SPH) simulations of a Milky Way sized galaxy. The code takes into account hydrodynamics, self-gravity, star formation, supernova and stellar wind feedback, radiative cooling and metal enrichment. The simulated galaxy is a barred-spiral galaxy consisting of a stellar and gas disc, enveloped in a static dark matter halo. Similar to what is found in our pure N-body simulation of a non-barred galaxy in Grand et al. (2012), we find that the spiral arms are transient features whose pattern speeds decrease with radius, in such a way that the pattern speed is almost equal to the rotation of star particles. We trace particle motion around the spiral arms at different radii, and demonstrate that there are star particles that are drawn towards and join the arm from behind (in front of) the arm and migrate toward the outer (inner) regions of the disc until the arm disappears as a result of their transient nature. We see this migration over the entire radial range analysed, which is a consequence of the spiral arm co-rotating at all radii. The migration is shown to largely preserve circular orbits (within a few percent). We also demonstrate that there is no significant offset of different star forming tracers across the spiral arm, which is also inconsistent with the prediction of classical density wave theory.

Key words: galaxies: evolution - galaxies: kinematics and dynamics - galaxies: spiral - galaxies: structure

1 INTRODUCTION

The most well known theory of spiral arm structure is the so-called spiral density wave theory, which describes the spiral arms as quasi-stationary density waves (Lindblad 1960; Lin & Shu 1964) that rotate with the same pattern speed at every radius. The spiral arm can therefore be described by a wave function. To describe the spiral arm with a wave function is beneficial because it is then possible to extract analytic solutions of quantities such as the dispersion relation by use of Euler's equations of motion. For these solutions, the tight winding approximation is made, which would require very tight spirals whose pitch angles remain constant (see Athanassoula 1984 and references therein). Spiral galaxies have been discussed in the context of global density wave patterns (e.g. Amaral & Lepine 1997; Yano et al. 2002; Antoja et al. 2011; Lépine et al. 2011). Some studies argue the existence of long-lived patterns in their simulations (Donner & Thomasson 1994). However, the long-lived classic spiral density structure has never been reproduced self-consistently, and in all numerical simulations, the spiral arm is seen to be a transient structure (Sellwood 2011).

The transient property exhibited by simulated spiral arms has stimulated the emergence of new discussion of spiral arm evolution. A recent suggestion includes multiple wave modes of different pattern speeds that create the transient nature of spiral arms by constructively and destructively interfering with one another, thereby ensuring the growth and decay of the stellar density enhancement (e.g. Sellwood & Kahn 1991; Masset & Tagger 1997; Minchev & Quillen 2006; Roškar et al. 2011; Quillen et al. 2011).

Another possible explanation of the transient nature is the co-rotating spiral arm. Here, the spiral arm is considered to be rotating with the material at every radius. Naturally, the transient property of the arm is manifested by the winding, which propagates to breaks and bifurcations of the spiral arm. Such breaks in the spiral arm structure were found in Wada et al. (2011) and Grand et al. (2012), who performed high resolution N-body smoothed particle hydrodynamics (SPH) simulations (and in the latter case, pure N-body simulations) of an isolated spiral galaxy. They show that the pattern speed of the spiral arms decreases with radius, such that it follows the circular velocity of star particles.

The co-rotating spiral arm is found to have significant consequences on the radial migration of star parti-

* rjg2@mssl.ucl.ac.uk

cles. Grand et al. (2012) demonstrated a new type of systematic motion of star particles close to the spiral arm in their simulation, that leads to large, efficient radial migration of star particles all along the arm as opposed to the case of a single co-rotation radius (Lynden-Bell & Kalnajs 1972; Sellwood & Binney 2002). The star particles were shown to join the arm from both sides. Star particles behind (in front of) the arm were accelerated (decelerated) continually because the similar rotation speeds of the star particles and spiral arm allowed the migrating star particles to stay very close to the density enhancement of the spiral arm. This mechanism is responsible for the steady gain/loss of angular momentum of the migrating star particles, whereby the star particle is allowed to find a new equilibrium in a higher/lower energy circular orbit, without scattering kinematically. The star particles never crossed the arm as they migrated, and stopped migrating when the high amplitude of the density enhancement disappeared due to the transient nature of the arms. Because this simulation was an N-body simulation of a pure stellar disc with no bar or bulge, the only factor that could be responsible for the observed motion was the spiral arm features.

Complementary to numerical simulations, observational tests of the pattern speed have been made by Speights & Westpfahl (2011), who use the solutions to the Tremaine-Weinberg equations (Tremaine & Weinberg 1984) to perform statistical analysis on NGC 1365, and find the best solution to be a pattern speed that decreases as $1/r$ (see also Merrifield et al. 2005; Merrifield et al. 2006; Meidt et al. 2008; Meidt et al. 2009). Another test is the presence of (or lack of) a clear offset between different star forming tracers across a spiral arm. In the context of density waves, star particles should flow through the spiral arm (everywhere except at a co-rotation radius) if the pattern speed is constant. As gas flows into the spiral arm from behind the arm inside co-rotation and from in front of the arm outside co-rotation, it is compressed into molecular clouds. Stars are born from molecular clouds and age as they continue to flow relative to the arm, leaving a clear trail of stellar evolution (star forming tracers) from one side of the arm to the other. This has recently been tested for NGC 4321 by Ferreras et al (2012), who find no apparent offset between H_α and UV sources. Foyle et al. (2011) also find no offset in twelve nearby spiral galaxies by observing the star forming tracers HI and CO, $24\mu\text{m}$ emission and UV emission to trace atomic gas, molecular gas, enshrouded stars and young stars respectively. Both studies are evidence against long-lived spiral arms.

In this study, our aim is to build upon our previous study (Grand et al. 2012) that focused on N-body dynamics in a pure stellar disc, and extend this research on the spiral arm pattern speed and star particle dynamics in high resolution N-body/SPH simulations of a barred spiral galaxy. This will enable us to study the spiral arm and its effects in a more realistic context, and to determine whether or not the presence of gas, star formation and a bar produces any significant effect on particle motion that may be distinguished from those seen in the pure N-body simulation. In comparison to Grand et al. (2012), we present a more robust method for determining the apparent pattern speed of the spiral arm, and attention is given to the energy evolution of particles that undergo radial migration at many radii. Ad-

ditionally, we show the distribution of young star particles of different ages to check for offsets in different star forming tracers. Although the analysis could be extended to the bar region, this paper focuses on the spiral arm. Hence we leave the analysis of the structure and evolution of bars to future studies.

In Section 2, a description of the SPH code is given before the model set up and the chosen initial parameters are outlined. In Section 3 we present the results of our analysis, compare them with previous studies and discuss their implications. In Section 4 we summarise the significance of the results and remark upon the value of the simulations and future work.

2 METHOD AND MODEL SETUP

2.1 GCD+ code

In our simulation, we use an updated version of the original galactic chemodynamical evolution code, GCD+, developed by Kawata & Gibson (2003). A detailed description of the code is seen in Rahimi & Kawata (2011). Here we give a brief outline. GCD+ is a three-dimensional tree N-body/SPH code (Gingold & Monaghan 1977; Lucy 1977; Barnes & Hut 1986; Hernquist & Katz 1989; Katz et al. 1996) that incorporates self-gravity, hydrodynamics, radiative cooling, star formation, supernova feedback and metal enrichment. This latest version of GCD+ takes into account metal diffusion as suggested by Greif et al. (2009). The scheme follows that of Rosswog & Price (2007): we use their artificial viscosity switch (Morris 1997) and artificial thermal conductivity to resolve Kelvin-Helmholtz instabilities (Kawata et al. 2009). Further adaptations include those of adaptive softening (Price & Monaghan 2007) and an individual time step limiter (Saitoh et al. 2008) in order to correctly resolve particle response to shock layers ploughing through material from supernova and wind blown bubbles (e.g. Merlin et al. 2010; Durier & Dalla Vecchia 2011).

Radiative cooling and heating is calculated with CLOUDY (v08.00: Ferland et al. 1998). UV background radiation is also taken into account (Haardt & Madau 1996). Our star formation formula corresponds to the Schmidt law. We set a threshold density for star formation, n_{th} , which means that star formation will occur for any region that exceeds this density and the velocity field is convergent.

We assume that stars are distributed according to the Salpeter (1955) initial mass function (IMF). Chemical enrichment by both Type II (Woosley & Weaver 1995) and Type Ia supernovae (Iwamoto et al. 1999; Kobayashi et al. 2000) and mass loss from intermediate-mass stars (van den Hoek & Groenewegen 1997) are taken into account. The new version of GCD+ uses a different scheme for star formation and feedback (see Rahimi & Kawata 2011). We now keep the mass of the baryon (gas and star) particles completely the same, unlike our old version (Kawata & Gibson 2003) or the majority of SPH simulations which include star formation.

The main parameters that govern star formation and supernova feedback (Rahimi & Kawata 2011) are set as follows: the star formation density threshold, $n_{th} = 1.0 \text{ cm}^{-3}$; star formation efficiency, $C_* = 0.1$; supernova energy input, $E_{SN} = 10^{50} \text{ erg}$ per supernova; and stellar wind energy

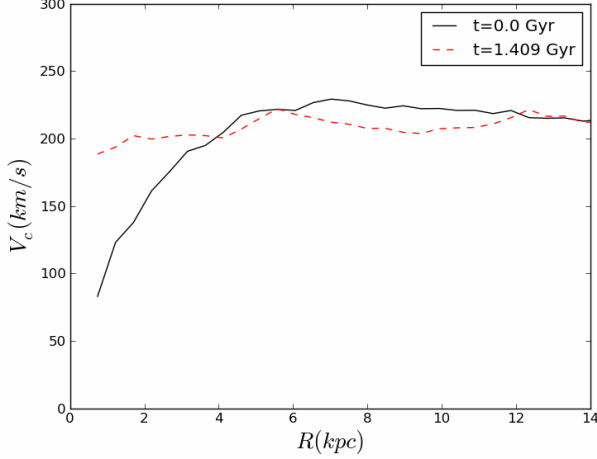


Figure 1. The initial circular velocity (solid black line) and the circular velocity at $t = 1.409$ Gyr (dot-dashed red line).

input, $E_{\text{SW}} = 10^{36} \text{ erg s}^{-1}$. Each particle in the simulation is assigned a unique ID number. This makes it easy to trace any particle during the evolution of the simulation.

2.2 Simulation Setup

Our simulated galaxy consists of a spherical static dark matter halo and two live discs: a stellar disc and a gas disc. The dark matter halo density profile follows that of Navarro et al. (1997):

$$\rho_{\text{dm}} = \frac{3H_0^2}{8\pi G} (1+z_0)^3 \frac{\Omega_0}{\Omega(z)} \frac{\rho_c}{cx(1+cx)^2}, \quad (1)$$

where ρ_c is the characteristic density described by Navarro et al. (1997), the concentration parameter, $c = r_{200}/r_s$, and $x = r/r_{200}$. The scale length is r_s , and r_{200} is the radius inside which the mean density of the dark matter sphere is equal to $200\rho_{\text{crit}}$ (where $\rho_{\text{crit}} = 3H_0^2/8\pi G$; the critical density for closure):

$$r_{200} = 1.63 \times 10^{-2} \left(\frac{M_{200}}{h^{-1} M_\odot} \right)^{\frac{1}{3}} \left[\frac{\Omega_0}{\Omega(z_0)} \right]^{-\frac{1}{3}} (1+z_0)^{-1} h^{-1} \text{kpc}. \quad (2)$$

We assume $M_{200} = 1.5 \times 10^{12} M_\odot$, $c = 10$, $\Omega_0 = 0.266$, $z_0 = 0$ and $H_0 = 71 \text{ km s}^{-1} \text{ Mpc}^{-1}$.

The stellar disc is assumed to follow an exponential surface density profile:

$$\rho_{d,*} = \frac{M_{d,*}}{4\pi z_{d,*} R_{d,*}} \text{sech}^2 \left(\frac{z}{z_{d,*}} \right) \exp \left(-\frac{R}{R_{d,*}} \right), \quad (3)$$

where the disc mass, $M_{d,*} = 5 \times 10^{10} M_\odot$, the scale length, $R_{d,*} = 2.5 \text{ kpc}$ and the scale height $z_{d,*} = 0.35 \text{ kpc}$, which is constant over the disc. The velocity dispersion for each three dimensional position of the disc is computed following Springel et al. (2005) to construct the almost equilibrium initial condition. One free parameter in this method is the ratio of the radial velocity dispersion to the vertical velocity dispersion, f_R , which relates as $f_R = \sigma_R/\sigma_z$. We choose

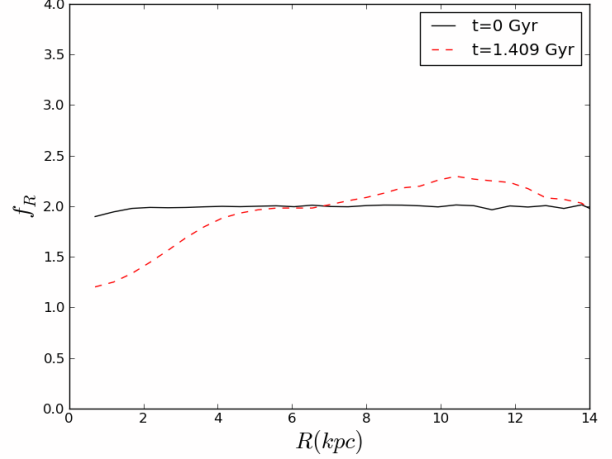


Figure 3. The ratio of velocity dispersions in the radial and z direction, $f_R = \sigma_R/\sigma_z$, at $t = 0$ (solid black line) and $t = 1.409$ Gyr (dashed red line), plotted as a function of radius.

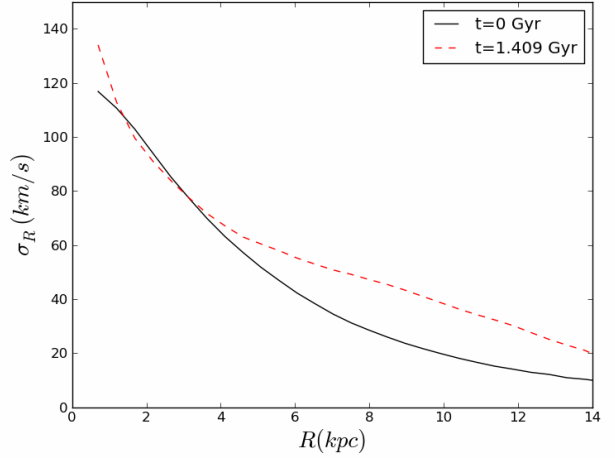


Figure 4. Radial velocity dispersion computed at $t = 0$ (solid black line) and $t = 1.409$ Gyr (dashed red line), as a function of radius.

$f_R = 2$ in the simulation shown. The initial circular velocity curve is shown in Fig. 1 (solid line). The initial rotation speed at 8 kpc is $\sim 230 \text{ km s}^{-1}$.

The gas disc is set up following the method described in Springel et al. (2005). The radial surface density profile is assumed to follow an exponential law like the stellar disc. The initial vertical distribution of the gas is iteratively calculated to be in hydrostatic equilibrium assuming the equation of state calculated from our assumed cooling and heating function. For the gas disc, we set the disc mass, $M_{d,g} = 1 \times 10^{10} M_\odot$, the scale length, $R_{d,g} = 4.0 \text{ kpc}$.

We use $N_{d,*} = 2 \times 10^6$ and $N_{d,g} = 4 \times 10^5$ particles for stars and gas respectively, and therefore the mass of each particle is $2.5 \times 10^4 M_\odot$. Fujii et al. (2011) show that if more than one million particles are used to describe the disc component, artificial heating that suppresses the spiral arm formation is not significant. Our simulation uses a total

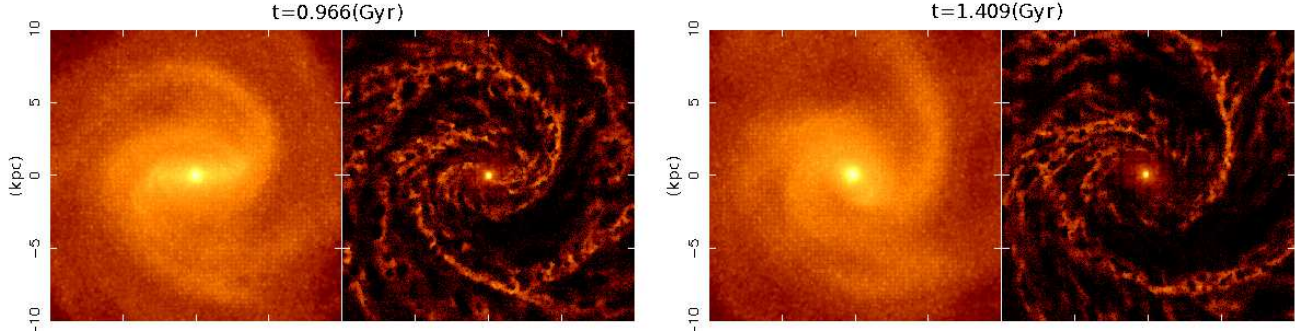


Figure 2. Snapshots of the face-on view of the simulated galaxy at $t = 0.966$ Gyr (left) and $t = 1.409$ Gyr (right). The left images show the stellar density map, and the right images show the gas density map. The bar is strong at the earlier time, and becomes more stable at the later time.

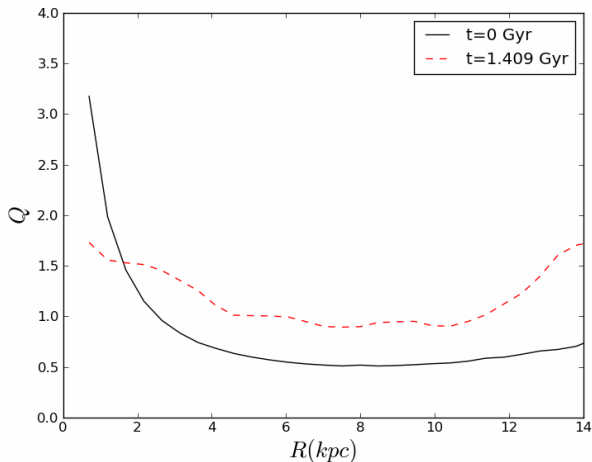


Figure 5. Toomre's instability parameter, Q , computed at $t = 0$ (solid black line) and $t = 1.409$ Gyr (dashed red line), as a function of radius.

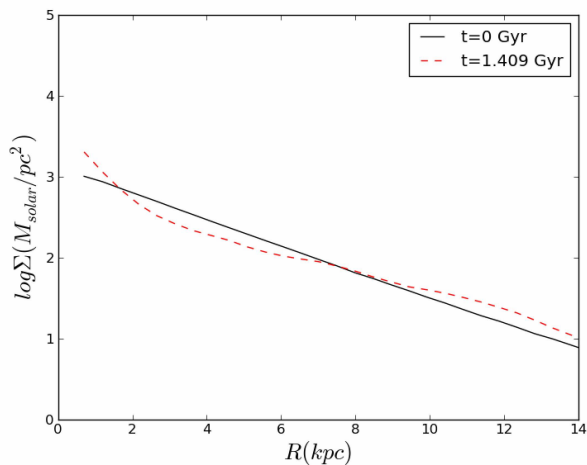


Figure 6. Logarithm of the surface density, computed at $t = 0$ (solid black line) and $t = 1.409$ Gyr (dashed red line), as a function of radius.

of 2.4×10^6 particles and therefore is expected to be less affected by artificial heating. We adopt a softening length equal to the smoothing length but set the minimum softening length to 340 pc for gas particles and apply a fixed softening length of 340 pc for star particles, with the spline softening suggested by Price & Monaghan (2007). These parameters of the stellar component are similar to that of the non-barred spiral galaxy simulated in Grand et al. (2012), but with a higher disc to halo mass ratio. To induce spontaneous bar formation (e.g. Ostriker & Peebles 1973), we have applied a lower concentration parameter, $c = 10$, in eq. (1).

3 RESULTS AND DISCUSSION

The simulation set up in Section 2 was evolved for 2 Gyr. The stellar and gas component is shown at two different times in Fig. 2, and we see a prominent bar spiral structure in both components. The strong bar develops around $t = 0.966$, and settles to a smaller bar before $t = 1.409$ Gyr. Similar to previous studies described in Section 1, we also find that the disc develops transient and recurrent spiral arms. In this paper, we focus our analysis around the arm at $t = 1.409$ Gyr because this is a prominent one, which facilitates our analysis and we are able to extract and more clearly demonstrate the key features that we want to identify, namely the pattern speed and the particle motion around the spiral arm.

The circular velocity at $t = 0$ and $t = 1.409$ Gyr is shown in Fig. 1. The circular velocity in the inner region at the later time is significantly different from that of the earlier time, owing to the strong gravitational field created by the developed bulge. Fig. 3 shows f_R as a function of radius at $t = 0$ and $t = 1.409$ Gyr. The value drops with time in the inner radii (bar region). Outside $R \sim 5$ kpc, f_R increases slightly as the disc is heated by strong spiral structure, which increases the velocity dispersion, σ_R , shown explicitly in Fig. 4. The effect on spiral structure is quantified in Fig. 5, which shows an increase of Toomre's instability parameter, $Q = \sigma_R \kappa / 3.36 G \Sigma_*$, in the spiral region, where κ is the epicycle frequency and Σ_* is the surface density of the stellar component. This is contrary to the bar region where Q is lowered owing to the large surface density excess in the central region shown in Fig. 6. A bulge that creates this excess of central density are likely formed through sec-

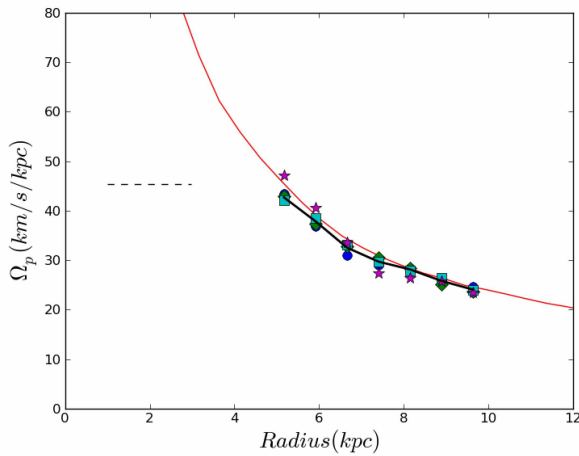


Figure 8. The bar and spiral arm pattern speed calculated for the snapshots shown in Fig. 7. The spiral arm pattern speed (solid black line) is averaged over several pattern speeds calculated at different snapshots over the course of the spiral arm’s evolution. Four of them are shown by the different coloured symbols. The circular velocity is also plotted (solid red line). The bar pattern speed (dashed black line) is found to be $45 \text{ km s}^{-1} \text{ kpc}^{-1}$. The spiral pattern speed exhibits a decreasing trend with radius that is similar to the circular velocity. Similar trends are found at other time steps with different arms.

ular evolution caused by the bar (e.g. Pfenniger & Norman 1990; Kormendy & Kennicutt 2004 and references therein). The developed bulge is apparent in Fig. 2.

As in Grand et al. (2012), our analysis and discussion will focus around one epoch, centred on $t \sim 1.409 \text{ Gyr}$. It should be noted however, that we also applied similar analyses to other spiral arms that developed at different times in this simulation as well as spiral arms in other barred spiral simulations with different initial configurations of the disc and dark matter halo. We find that all the spiral arms we analysed show very similar results to those shown in this section (see also Kawata et al. 2012).

First, we present the analysis and results of the pattern speeds of the chosen spiral arm. Then we examine the motion of selected particles around the arm, and present and discuss an analysis of their angular momentum and energy evolution. We also examine the position of star particles of different ages in and around the spiral arm, which would be an observational test for pattern speeds of spiral arms (Tamburro et al. 2008; Egusa et al. 2009; Foyle et al. 2011; Ferreras et al. 2012). If the spiral arms rotate with a constant pattern speed, systematic offsets in azimuth between age populations and the spiral arm as a function of radii are expected.

3.1 Pattern Speed

Here we present a method for calculating the rate at which the stellar density enhancement rotates as a function of radius i.e. the pattern speed. The pattern speeds are often measured by spectrogram analysis (e.g. Quillen et al. 2011). However, we focus on the angular pattern speed of the apparent spiral feature, and in this paper we refer to this as

the pattern speed. The location of the stellar density peak is found at a range of radii for a series of snapshots. This is done by weighting the positional information of particles close to the arm by their density. First, an azimuth coordinate is chosen close to the peak as an initial guess at a given radius. Then, a suitable azimuthal range centred on the initial guess is applied to select the particles covering the whole spiral arm or bar. From the selected particles at a given radius, we calculate:

$$\bar{\theta}_{sp}(r) = \frac{\sum_i^N \rho_i \theta_i(r)}{\sum_i^N \rho_i(r)}. \quad (4)$$

Here, θ_i and ρ_i are the azimuth angle and stellar density at the position of the i -th star particle. We iteratively find $\bar{\theta}_{sp}(r)$, narrowing the sampling range of θ progressively. The peak density of the spiral arm ($5 < R < 10 \text{ kpc}$) and the bar ($1 < R < 3 \text{ kpc}$) is shown in Fig. 7. The bar and spiral features are split in this way because of difficulty in tracing the density peak in the intermediate region ($3 < R < 5 \text{ kpc}$).

The angular pattern speed is measured several times from snapshots like those in Fig. 7, and averaged. The results are plotted in Fig. 8. The pattern speed of the spiral arm decreases with radius, such that it almost equals the angular circular velocity of star particles (circular velocity in Fig. 1 at $t = 1.409 \text{ Gyr}$ for reference) in the disc at all radii. This indicates that this spiral arm feature appears to be co-rotating, which is consistent with the short lifetime of the spiral arm ($\tau_{sp} \sim 160 \text{ Myr}$). This is confirmed from the snapshots of our simulation in Fig. 7.

The transient and co-rotating spiral arm is consistent with Wada et al. (2011) and Grand et al. (2012), who also find that the spiral arm features in their simulations are co-rotating, winding and short-lived. Our simulation shows that the transient and co-rotating spiral arms are seen in barred galaxy simulations as well (see also Baba et al. 2009).

3.2 Radial Migration around the spiral arm

Radial migration at the co-rotation radius has been predicted to preserve the circular motion of orbits i.e. not to heat them kinematically (e.g. Lynden-Bell & Kalnajs 1972; Sellwood & Binney 2002; Roškar et al. 2008; Sánchez-Blázquez et al. 2009; Roškar et al. 2011; Minchev & Famaey 2010; Minchev et al. 2011; Brunetti et al. 2011). A direct implication of a co-rotating spiral arm is that there are co-rotation radii all over the disc, and so the radial migration is expected to occur at a wide range of radii of the spiral arm. This is consistent with Grand et al. (2012), where this was shown for a pure N-body stellar disc that developed only spirals (no bar).

First, we select a sample of particles around our chosen arm of interest at a given radius in the $t = 1.409 \text{ Gyr}$ snapshot in Fig. 2. In order to focus on star particles that are likely affected by the spiral arm, the particle sample is selected to be within the vertical height of $|z| < 200 \text{ pc}$ and azimuthal width of 4 kpc centred on highest density point of the arm i.e. a given radius of the peak line shown in Fig. 7. The radial thickness of the sample is chosen to be 0.25

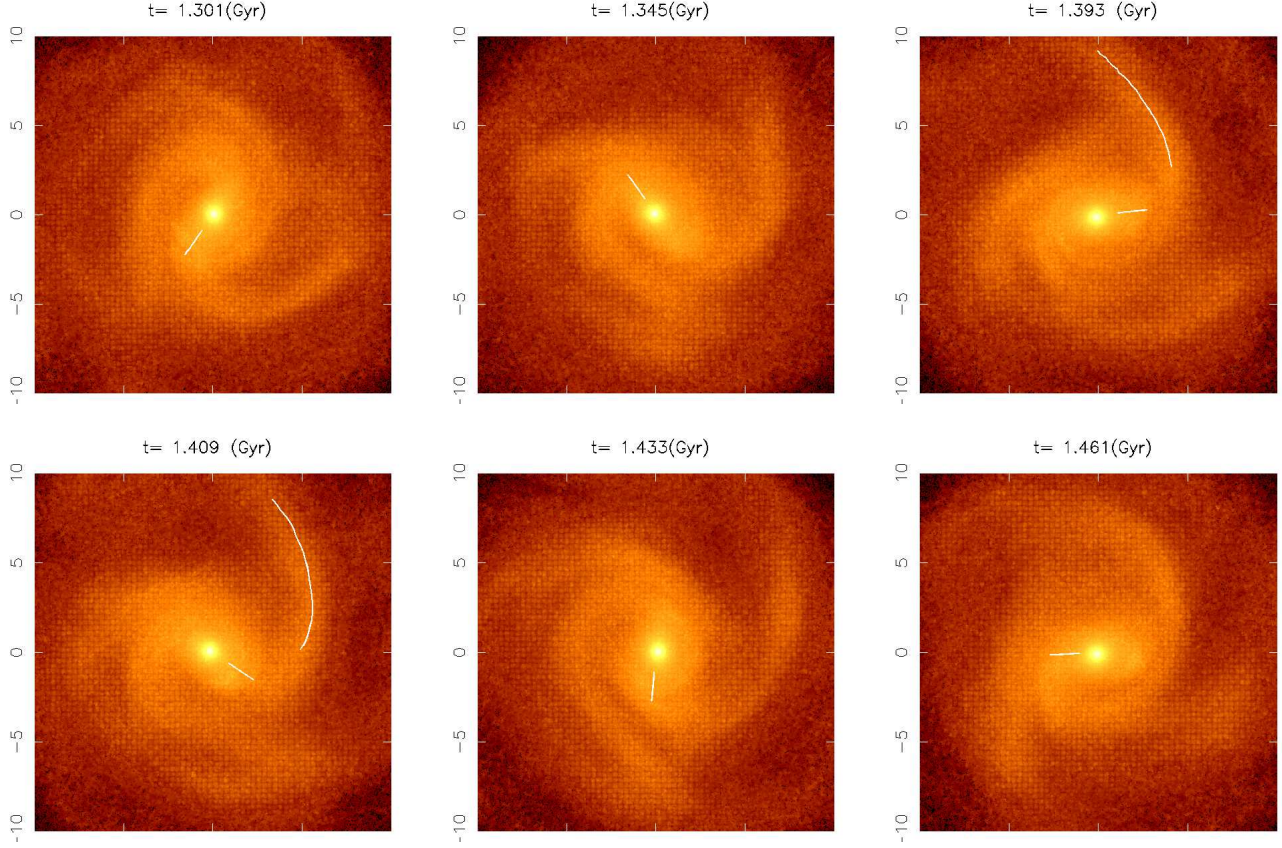


Figure 7. Snapshots of the galaxy from $t = 1.301$ to $t = 1.461$ Myr. In each snapshot, the white lines mark out the position of highest density over the spiral arm as a function of radius found from the method described in the text. The line marking the bar and spiral arm position (*top-right* and *bottom-left* snapshots only) focused on in this paper extends from 1 – 3 kpc and 5 – 10 kpc respectively. These snapshots also show that the spiral arm is winding and the lifetime of the spiral arm is roughly $\tau_{sp} \sim 160$ Myr.

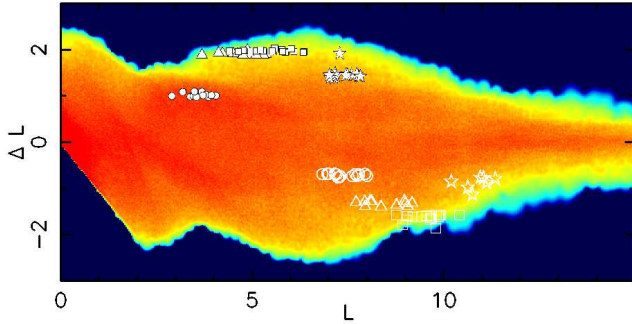


Figure 9. The angular momentum at the beginning of the time period examined, L , plotted against the change in angular momentum over 80 Myr, ΔL . The smoothed colour map from low number density (dark blue) to high number density (red) incorporates all disc star particles, and shows a broad angular momentum range for migration. Selected positive (filled symbols) and negative (open symbols) extreme migrators (see text) are highlighted by circle (chosen at a radius of ~ 6 kpc), triangle (~ 7 kpc), square (~ 8 kpc) and star (~ 9 kpc) symbols. Units are arbitrary.

kpc to ensure that a large sample of stars of approximately the same radius are chosen.

From the selected sample of particles, we compute the

angular momentum change, ΔL , over a period of 80 Myrs and choose those that exhibit the largest values of $|\Delta L|$, some of which are highlighted by symbols in Fig. 9. As a fraction of their initial angular momentum, L , this can be up to as much as $|\Delta L/L| \simeq 50\%$. Note that the angular momentum exchanges in this simulation are much stronger than those of Grand et al. (2012), probably because the spiral arm structure is much more prominent in this barred spiral galaxy. The radii of the guiding centres of these high $|\Delta L|$ particles highlighted in Fig. 9 change significantly i.e. they migrate radially. We call these strongly migrating particles 'extreme migrators', and further divide them into two subcategories: positive extreme migrators and negative extreme migrators for particles that gain and lose the angular momentum in the sample respectively.

In Fig. 10 we show three successive snapshots during the migration period of the four extreme migrator samples highlighted in Fig. 9, each selected around radii of 6, 7, 8 and 9 kpc (positive and negative migrators are denoted by filled and open symbols respectively, where each type of symbol corresponds to a specific selection radius of a sample): 20 Myr before selection (top panel), at selection (middle panel) and 20 Myr after selection (bottom panel). The density snapshots for the stellar component are coordinate transformed from cartesian to polar in order to make the radial motion of the selected star particles with respect to

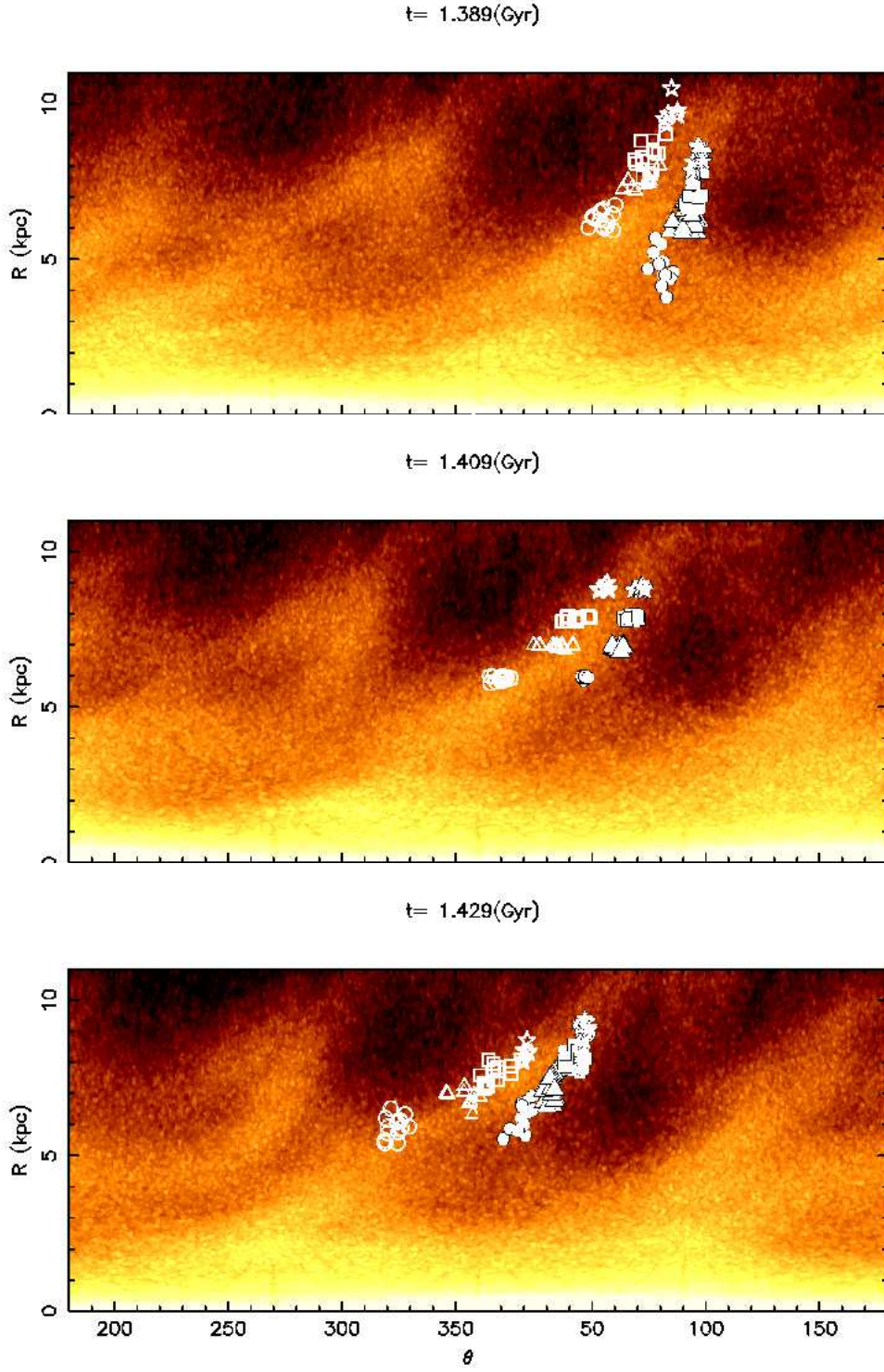


Figure 10. Stellar density distribution plotted in polar coordinates showing the time evolution of four sets of extreme migrator selected from particle samples around radii of 6, 7, 8 and 9 kpc at $t = 1.409$ Gyr snapshot. The symbols correspond to those of Fig. 9. Azimuth (θ) is expressed in degrees. The particles have migrated toward outer radii on the trailing edge of the spiral arm and inwards on the leading edge.

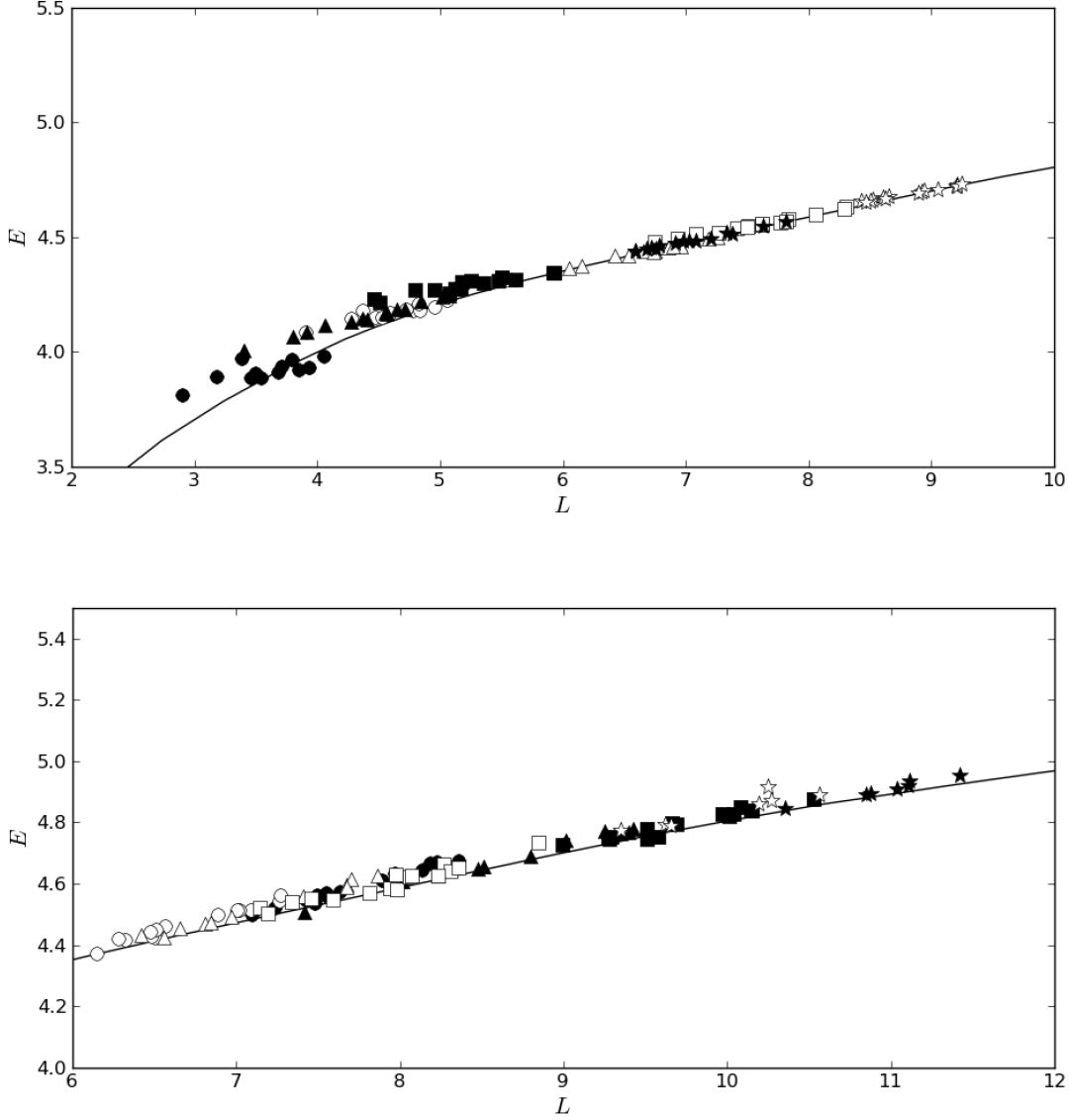


Figure 11. The energy, E , and angular momentum, L , distribution of the extreme migrators in Fig. 10 at 40 Myr before (filled symbols) and 40 Myr after (open symbols) the time step at which they were selected. Each symbol represents a specific radius of selection corresponding to Fig. 10. The top (bottom) panel shows the results of the migrators that moved toward the outer (inner) radii. The solid black line indicates the circular orbit. Units are arbitrary.

the arm clearer. The positive migrators are always seen on the trailing side of the spiral arm and migrate towards the outer radii. They are trapped by the potential of the spiral arm, which accelerates them. The co-rotating nature of the spiral arm feature ensures that during migration to outer radii, instead of passing through the spiral arm they remain in the vicinity of the arm on the trailing side. Therefore, they continue to be accelerated until the spiral arm is disrupted. The negative migrators are particles that migrate towards the inner radii on the leading side of the spiral arm. They are decelerated as they become caught in the potential of the spiral arm, and because of the co-rotating feature, they continue to decelerate on the leading side, again until the spiral arm is disrupted. This illustrates the different sys-

tematic motion that occurs on each side of the spiral arm, which is reminiscent of the behaviour found in Grand et al. (2012). The analysis here demonstrates that the presence of a bar does not alter this behaviour.

3.3 Angular momentum and energy evolution

The orbital energy of a star particle can be affected by the gain and loss of angular momentum associated with radial migration. As in Grand et al. (2012) and following Sellwood & Binney (2002), we calculate the energy, E , and angular momentum, L , of the extreme migrators in Fig. 10 at 40 Myr before and after the time step at which they were selected. We call these two time steps the 'initial' and

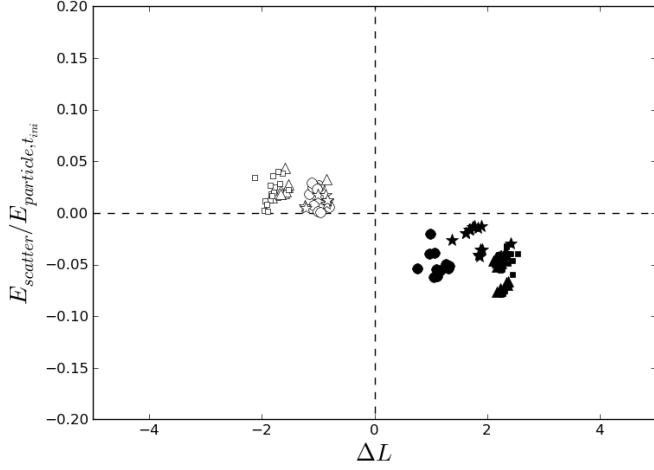


Figure 12. The groups of migrators shown in Fig. 11 are plotted here in the $\Delta L - E_{\text{scatter}}/E_{\text{particle},t_{\text{ini}}}$ plane, where E_{scatter} is the change in the quantity defined by $E_{\text{particle},t} - E_{\text{circ}}$ between the initial and final time. $E_{\text{particle},t}$ is the total particle energy at a given time and E_{circ} is the energy of a test particle of circular orbit for the given angular momentum (i.e. the minimum orbital energy allowed). $E_{\text{scatter}}/E_{\text{particle},t_{\text{ini}}}$ tells us how much the star particle has gained or lost random energy as a fraction of the initial particle energy during the migration process. We can see the positive (filled symbols) and negative (open symbols) migrators lie in distinct groups, where the former are *cooled* and the latter *heated*, but only by a relatively small amount.

'final' time steps respectively. In Fig. 11 we show the position of the extreme migrators at the initial (filled symbols) and final (open symbols) time steps for all migrator samples in Fig. 9. The solid black line indicates the L and E expected for a pure circular orbit at each radius. This represents the minimum energy which a star particle can have at a given angular momentum. We see that the positive migrators (top panel) and negative migrators (bottom panel) move along the circular velocity curve in opposite directions to each other. Because they keep close to the circular velocity curve after migration, their orbits must retain their near circularity, and they gain (or lose) little random energy and are not scattered into higher energy orbits (Sellwood & Binney 2002). In other words, their kinematically cool orbits are largely preserved.

To quantify this, Fig. 12 shows the amount of non-circular kinetic energy change (normalised to total initial energy) over the migration period plotted as a function of the amount of angular momentum change that they have undergone. It is clear that each type of migrator is grouped separately, such that the positive migrators become slightly cooler, and negative migrators become slightly hotter (see also Grand et al. 2012; Roškar et al. 2011), although this is only a few percent of the initial energy.

3.4 Stellar population distribution around spiral arms

Because we have a gas component forming stars, we can now make a further test of whether the spiral arms are long-lived

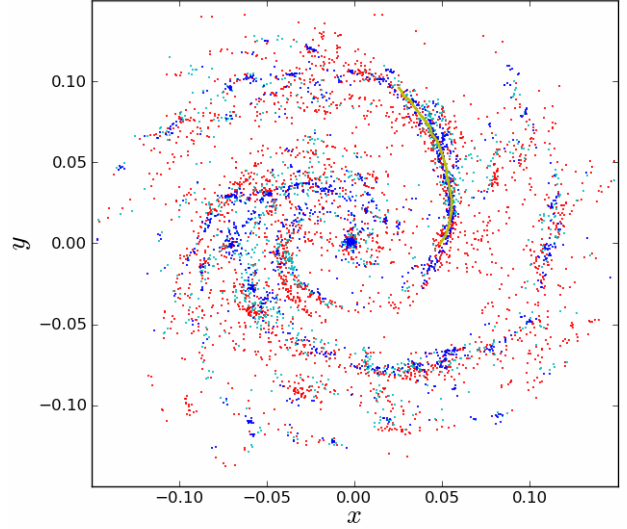


Figure 13. Snapshot of the disc at $t = 1.409$ Gyr, showing only star particles of age: $t < 50$ Myr (blue); $50 < t < 100$ Myr (cyan); $100 < t < 200$ Myr (red). The yellow line indicates the stellar peak density shown in Fig. 7.

density waves as in spiral density wave theory. The long-lived, stationary wave theory should predict clear azimuthal offsets between young star particles of different ages, and molecular clouds (MCs) that are the seeds of star formation. The single constant pattern speed predicted by this theory would mean that inside the co-rotation radius, gas and stars would be moving faster than the spiral arm feature. Then gas flows into the spiral arm from behind the arm, and is compressed into MCs. This leads to star formation. Newly born stars will then flow through and begin to overtake the arm feature as they age, which naturally leads to a temporal gradient over the spiral arm. Outside of co-rotation, where material moves slower than the spiral arm feature, the opposite temporal gradient is expected. Therefore, if we group star particles around the spiral arm into age bins, and examine their azimuthal distribution there should be apparent azimuthal offsets among star particles of different ages, which would become clearer further from co-rotation. Dobbs & Bonnell (2008) and Dobbs & Pringle (2010) performed a similar test by embedding a rigidly rotating spiral potential with a constant pattern speed.

We also analyse the azimuthal distribution of stellar ages found in our simulated galaxy. Note that although Dobbs & Pringle (2010) show similar analysis, they do not explicitly include radiative cooling or star formation, but assume an isothermal gas. They track the orbit of gas particles which have experienced the high density state, after which time the gas particles are tracked as very young stars ($2 - 100$ Myr), assuming the gas and stellar dynamics are similar in this short period. Therefore, our study is different and complementary. Fig. 13 shows the distribution of a young population, $t_{\text{age}} < 50$ Myr (blue); an intermediate population, $50 < t_{\text{age}} < 100$ Myr (cyan); and a relatively older population, $100 < t_{\text{age}} < 200$ Myr (red). The snapshot shown is at $t = 1.409$ Gyr. Inspection by eye indicates

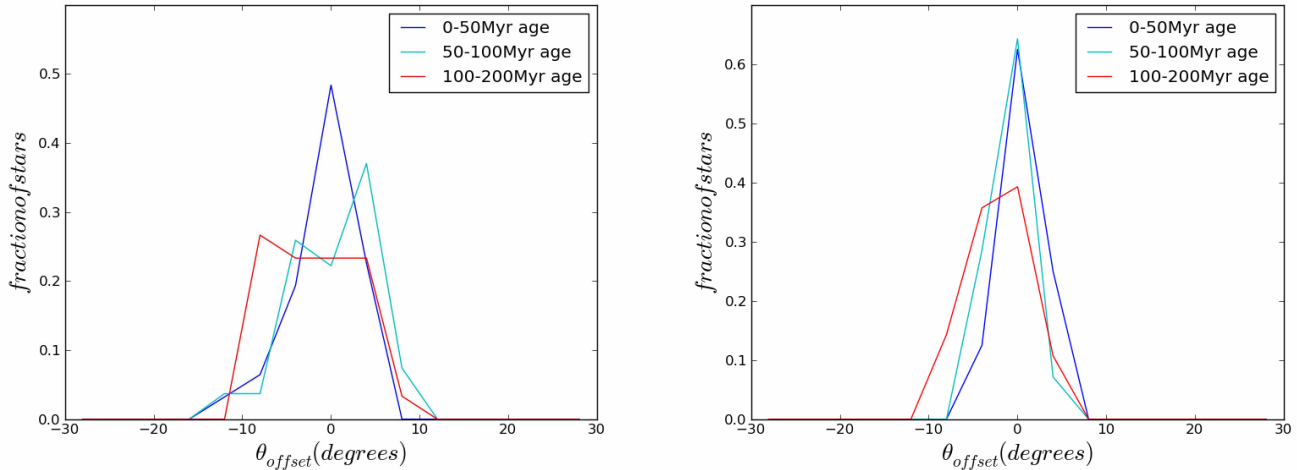


Figure 14. Histogram binning star particles from sample in 6 to 6.5 kpc range (left) and 7.5 to 8 kpc range (right) according to their azimuthal offset from the peak density line shown in Fig. 13. Negative offsets refer to the trailing side of the arm, and positive offsets refer to the leading side. No systematic offset of stellar ages is apparent.

that there is no obvious offset present. To quantify this, we select two samples of star particles: one between 6 and 6.5 kpc radius and the other between 7.5 and 8 kpc radius, each within ± 2 kpc from the peak density of the spiral arm in the azimuthal direction. The angular offset distribution from the peak density for selected star particles of different ages are shown in Fig. 14, where the abscissa is azimuth offset angle and the ordinate is the number fraction of star particles. A negative angular offset is taken to mean a position behind the spiral arm, and a positive one means a position in front of the spiral arm. In both cases, no significant offset is seen between star particles of different ages: all age groups peak around zero offset, indicating that the majority of star particles formed in the spiral arm co-rotate with the spiral arm. Neither case finds any systematic spatial offset that would be present if the arm was a density wave. It is clear that the distribution broadens for older star particles, although the peak position remains at zero offset. Our results are qualitatively similar to the results of the flocculent and interacting galaxy cases in Dobbs & Pringle (2010)¹. Expectedly, it is completely different from their fixed pattern speed case.

4 CONCLUSIONS

We have presented three dimensional N-body/SPH simulations of an isolated barred spiral galaxy, and performed a dynamical analysis of the spiral arms and particles around the spiral arms, tracing their evolution and the azimuthal distribution of star particles as a function of age. We come to the following conclusions:

(i) We find in our simulation that spiral arms are transient recurring features: we observe the continuous disappearance of spiral arms and the reappearance of new ones. This transient nature has always been found in numerical simulations.

(ii) Our result shows a convincing coincidence of circular velocity and pattern speed at all radii shown (outside the bar region), which supports a co-rotating picture of the spiral arm. This is reflected in points iii), iv) and v), and consistent with what is found in Wada et al. (2011) and Grand et al. (2012) for non-barred spiral galaxy simulations. This is contrary to classic spiral density wave theory, in which there is a constant pattern speed independent of radius, and hence *only one* co-rotation radius.

(iii) Particles are shown to join the spiral arm at all radii from both behind and in front of the arm. As in Grand et al. (2012), we observe the particles joining from the trailing (leading) side of the spiral arm and their continued migration to outer (inner) radii thanks to the continued acceleration (deceleration) offered by the co-rotating spiral arm. The migrators keep close to and slide along the spiral arm on both sides as time evolves, and do not pass through, are passed by, nor appear to recoil away from the spiral arm in a manner similar to horseshoe orbits.

(iv) We quantify the amount of heating or cooling of each migrator in terms of random energy gained or lost over the process of migration. It is evident that each positive migrator loses some random energy (cools), while the negative migrators gain some random energy (heated). For each migrator, it is seen that the amount of heating/cooling is at most a few percent of the total energy of a given particle. Hence this migration does not contribute much to disc heating. However the cause of this heating and cooling is not identified (see also Roškar et al. 2011), and is worthy of further study.

(v) We find no offset between the distribution of young star particles (< 200 Myr) of different ages around the spiral

¹ Their barred galaxy case focuses on the stellar distribution around the bar not the spiral arm, and is therefore irrelevant to our discussion in this section.

arm at two different radii. This is consistent with recent observations of extra-galaxies (Foyle et al. 2011; Ferreras et al. 2012).

This study is a follow-up study to our previous paper Grand et al. (2012), which focused on pure N-body simulations of a galaxy with no bar. As in that study, we have not addressed the mechanism of formation of the spiral arm features thoroughly nor their destruction. We note that the spiral arm features here are slightly longer-lived than our N-body galaxy, which could be because the bar is a powerful driver of spiral structure (e.g. Sparke & Sellwood 1987), and may help to maintain the feature for longer (e.g. Donner & Thomasson 1994 Binney & Tremaine 2008; Baba et al. 2009, Quillen et al. 2011).

Again, we find that the spiral arms in this N-body/SPH barred galaxy are not consistent with the long-lived, rigidly rotating spiral arms of a classical spiral density wave theory. We have shown how this co-rotating nature of the spiral arm affects particle motion and their distribution around it. To observe significant radial migration around a single spiral arm over such a wide range of radii reassures the co-rotating nature of the spiral arm. Future studies should focus on testing this paradigm of the spiral arm with observations of our own Galaxy and of external galaxies (e.g. Meidt et al. 2009; Foyle et al. 2011; Speights & Westpfahl 2011; Ferreras et al. 2012), and comparing with simulations.

ACKNOWLEDGEMENTS

The authors acknowledge the support of the UK's Science & Technology Facilities Council (STFC Grant ST/H00260X/1). The calculations for this paper were performed on Cray XT4 at Centre for Computational Astrophysics, CfCA, of National Astronomical Observatory of Japan and the DiRAC Facility jointly funded by STFC and the Large Facilities Capital Fund of BIS. The authors acknowledge support of the STFC funded Miracle Consortium (part of the DiRAC facility) in providing access to the UCL Legion High Performance Computing Facility. The authors additionally acknowledge the support of UCL's Research Computing team with the use of the Legion facility. This work was carried out, in whole or in part, through the Gaia Research for European Astronomy Training (GREAT-ITN) network. The research leading to these results has received funding from the European Union Seventh Framework Programme ([FP7/2007-2013] under grant agreement number 264895).

REFERENCES

- Amaral L. H., Lepine J. R. D., 1997, *MNRAS*, 286, 885
 Antoja T., Figueras F., Romero-Gómez M., Pichardo B., Valenzuela O., Moreno E., 2011, *MNRAS*, 418, 1423
 Athanassoula E., 1984, *Phys. Rep.*, 114, 319
 Baba J., Asaki Y., Makino J., Miyoshi M., Saitoh T. R., Wada K., 2009, *ApJ*, 706, 471
 Barnes J., Hut P., 1986, *Nature*, 324, 446
 Binney J., Tremaine S., 2008, *Galactic Dynamics: Second Edition*. Princeton University Press
 Brunetti M., Chiappini C., Pfenniger D., 2011, *A&A*, 534, A75
 Dobbs C. L., Bonnell I. A., 2008, *MNRAS*, 385, 1893
 Dobbs C. L., Pringle J. E., 2010, *MNRAS*, 409, 396
 Donner K. J., Thomasson M., 1994, *A&A*, 290, 785
 Durier F., Dalla Vecchia C., 2011, *MNRAS*, p. 1701
 Egusa F., Kohno K., Sofue Y., Nakanishi H., Komugi S., 2009, *ApJ*, 697, 1870
 Ferreras I., Cropper M., Kawata D., Page M., Hoversten A. H., 2012, *MNRAS*, in press
 Ferland G. J., Korista K. T., Verner D. A., Ferguson J. W., Kingdon J. B., Verner E. M., 1998, *PASP*, 110, 761
 Foyle K., Rix H.-W., Dobbs C. L., Leroy A. K., Walter F., 2011, *ApJ*, 735, 101
 Fujii M. S., Baba J., Saitoh T. R., Makino J., Kokubo E., Wada K., 2011, *ApJ*, 730, 109
 Gingold R. A., Monaghan J. J., 1977, *MNRAS*, 181, 375
 Grand R. J. J., Kawata D., Cropper M., 2012, *MNRAS*, p. 2358
 Greif T. H., Glover S. C. O., Bromm V., Klessen R. S., 2009, *MNRAS*, 392, 1381
 Haardt F., Madau P., 1996, *ApJ*, 461, 20
 Hernquist L., Katz N., 1989, *ApJS*, 70, 419
 Iwamoto K., Brachwitz F., Nomoto K., Kishimoto N., Umeda H., Hix W. R., Thielemann F.-K., 1999, *ApJS*, 125, 439
 Katz N., Weinberg D. H., Hernquist L., 1996, *ApJS*, 105, 19
 Kawata D., Gibson B. K., 2003, *MNRAS*, 340, 908
 Kawata D., Grand R. J. J., Cropper M., 2012, *Assembling the Puzzle of the Milky Way*, Le Grand-Bornand, France, Edited by C. Reylé; A. Robin; M. Schultheis; EPJ Web of Conferences, Volume 19, id.07006, 19, 7006
 Kawata D., Okamoto T., Cen R., Gibson B. K., 2009, *ArXiv e-prints*
 Kobayashi C., Tsujimoto T., Nomoto K., 2000, *ApJ*, 539, 26
 Kormendy J., Kennicutt Jr. R. C., 2004, *ARA&A*, 42, 603
 Lépine J. R. D., Roman-Lopes A., Abraham Z., Junqueira T. C., Mishurov Y. N., 2011, *MNRAS*, 414, 1607
 Lin C. C., Shu F. H., 1964, *ApJ*, 140, 646
 Lindblad P. O., 1960, *Stockholms Observatoriums Annaler*, 21, 4
 Lucy L. B., 1977, *AJ*, 82, 1013
 Lynden-Bell D., Kalnajs A. J., 1972, *MNRAS*, 157, 1
 Masset F., Tagger M., 1997, *A&A*, 322, 442
 Meidt S. E., Rand R. J., Merrifield M. R., 2009, *ApJ*, 702, 277
 Meidt S. E., Rand R. J., Merrifield M. R., Shetty R., Vogel S. N., 2008, *ApJ*, 688, 224
 Merlin E., Buonomo U., Grassi T., Piovani L., Chiosi C., 2010, *A&A*, 513, A36
 Merrifield M. R., Rand R. J., Meidt S. E., 2005, in *American Astronomical Society Meeting Abstracts Vol. 37 of Bulletin of the American Astronomical Society, Measuring Pattern Evolution: Winding Spiral Structure and Counter-Rotating Double Bars*. p. 1313
 Merrifield M. R., Rand R. J., Meidt S. E., 2006, *MNRAS*, 366, L17
 Minchev I., Famaey B., 2010, *ApJ*, 722, 112
 Minchev I., Famaey B., Combes F., Di Matteo P., Mouhcine M., Wozniak H., 2011, *A&A*, 527, A147

- Minchev I., Quillen A. C., 2006, MNRAS, 368, 623
- Navarro J. F., Frenk C. S., White S. D. M., 1997, ApJ, 490, 493
- Ostriker J. P., Peebles P. J. E., 1973, ApJ, 186, 467
- Pfenniger D., Norman C., 1990, ApJ, 363, 391
- Price D. J., Monaghan J. J., 2007, MNRAS, 374, 1347
- Quillen A. C., Dougherty J., Bagley M. B., Minchev I., Comparetta J., 2011, MNRAS, 417, 762
- Rahimi A., Kawata D., 2011, ArXiv e-prints
- Rosswog S., Price D., 2007, MNRAS, 379, 915
- Roškar R., Debattista V. P., Quinn T. R., Stinson G. S., Wadsley J., 2008, ApJ, 684, L79
- Roškar R., Debattista V. P., Quinn T. R., Wadsley J., 2011, ArXiv e-prints
- Saitoh T. R., Daisaka H., Kokubo E., Makino J., Okamoto T., Tomisaka K., Wada K., Yoshida N., 2008, PASJ, 60, 667
- Salpeter E. E., 1955, ApJ, 121, 161
- Sánchez-Blázquez P., Courty S., Gibson B. K., Brook C. B., 2009, MNRAS, 398, 591
- Sellwood J. A., 2011, MNRAS, 410, 1637
- Sellwood J. A., Binney J. J., 2002, MNRAS, 336, 785
- Sellwood J. A., Kahn F. D., 1991, MNRAS, 250, 278
- Sparke L. S., Sellwood J. A., 1987, MNRAS, 225, 653
- Speights J. C., Westpfahl D. J., 2011, ApJ, 736, 70
- Springel V., Di Matteo T., Hernquist L., 2005, MNRAS, 361, 776
- Tamburro D., Rix H.-W., Walter F., Brinks E., de Blok W. J. G., Kennicutt R. C., Mac Low M.-M., 2008, AJ, 136, 2872
- Tremaine S., Weinberg M. D., 1984, ApJ, 282, L5
- van den Hoek L. B., Groenewegen M. A. T., 1997, A&AS, 123, 305
- Wada K., Baba J., Saitoh T. R., 2011, ApJ, 735, 1
- Woosley S. E., Weaver T. A., 1995, ApJS, 101, 181
- Yano T., Chiba M., Gouda N., 2002, A&A, 389, 143